Monthly Notices of the ROYAL ASTRONOMICAL SOCIETY

MNRAS **522,** 3898–3911 (2023)
Advance Access publication 2023 April 26

https://doi.org/10.1093/mnras/stad1230

J-PLUS: characterization of high-velocity stars in the second data release

F. Quispe-Huaynasi,[1★] F. Roig,[1] S. Daflon,[1] C. B. Pereira,[1] V. M. Placco,[2] F. Jiménez-Esteban,[3] F. J. Galindo-Guil,[4] A. Alvarez-Candal,[1,5,6] J. Alcaniz,[1] R. E. Angulo,[7,8] J. Cenarro,[4] D. Cristóbal-Hornillos,[4] R. Dupke,[1] A. Ederoclite,[4] C. Hernández-Monteagudo,[9,10] C. López-Sanjuan,[4] A. Marín-Franch,[4] M. Moles,[4] L. Sodré, Jr,[11] J. Varela[4] and H. Vázquez Ramió[4]

[1]*Observatório Nacional (ON), MCTI, Rua Gal. José Cristino 77, Rio de Janeiro, 20921-400, RJ, Brazil*
[2]*NSF's NOIRLab, 950 N. Cherry Ave., Tucson, AZ 85719, USA*
[3]*Departamento de Astrofísica, Centro de Astrobiología (CSIC-INTA), ESAC Campus, Camino Bajo del Castillo s/n, E-28692, Villanueva de la Cañada, Madrid, Spain*
[4]*Centro de Estudios de Física del Cosmos de Aragón (CEFCA), Unidad Asociada al CSIC, Plaza San Juan 1, E-44001, Teruel, Spain*
[5]*Instituto de Astrofísica de Andalucía, CSIC, Apt 3004, E-18080, Granada, Spain*
[6]*Instituto de Física Aplicada a las Ciencias y las Tecnologías, Universidad de Alicante, San Vicent del Raspeig, E-03080, Alicante, Spain*
[7]*Donostia International Physics Center (DIPC), Paseo Manuel de Lardizabal 4, E-20018, Donostia-San Sebastián, Spain*
[8]*IKERBASQUE, Basque Foundation for Science, E-48013, Bilbao, Spain*
[9]*Instituto de Astrofísica de Canarias (IAC), E-38205, La Laguna, Spain*
[10]*Departamento de Astrofísica, Universidad de La Laguna (ULL), E-38200, La Laguna, Spain*
[11]*Instituto de Astronomia, Geofísica e Ciências Atmosféricas, Universidade de São Paulo, Rua do Matão 1226, São Paulo, 05508-090, SP, Brazil*

Accepted 2023 April 18. Received 2023 April 15; in original form 2023 February 1

ABSTRACT

High-velocity stars in the Milky Way are related to extreme astrophysical phenomena. In this work, we characterize 28 stars with Galactocentric velocities higher than 400 $\mathrm{km\,s^{-1}}$ observed in the Javalambre Photometric Local Universe Survey Data Release 2 (J-PLUS DR2) survey. We combine J-PLUS photometry with astrometric data from the *Gaia* DR3 catalogue to analyse the kinematics, dynamics, and fundamental stellar parameters of these stars. Our results indicate that most of the 28 stars have typical behaviour and properties of halo stars, and some of them could be related to the disk population. Some of the halo stars may belong to known structures that originated from mergers of other systems with the Milky Way.

Key words: stars: fundamental parameters – stars: kinematics and dynamics – Galaxy: stellar content.

1 INTRODUCTION

With the release of data from the *Gaia* mission, the interest of the astronomical community in the high-velocity stars has been revived. However, this interest is not recent. For example, the early work by Oort (1922, 1924, 1926), known for his contributions to galactic dynamics, was actually related to high-velocity stars. Subsequently, many studies containing the term 'high-velocity stars' have been reported. These stars have been selected mainly based on their high proper motions and/or high radial velocities.

The origin of the unusual velocities of these stars has always been a topic of discussion, and several mechanisms have been proposed for it. Among others, we can mention: core-collapse explosion of a very massive stars (supernova type II) in binary systems (Zwicky 1957; Blaauw 1961); thermonuclear detonation of a white dwarf in binary systems (Przybilla et al. 2008; Shen et al. 2018); dynamical interactions in small clusters of massive stars (Poveda, Ruiz & Allen 1967); dynamical interaction of binary systems with the supermassive black hole located at the centre of the Galaxy, or Hills mechanism (Hills 1988); and tidal disruptions of dwarf galaxies by the Milky Way in the past (Abadi, Navarro & Steinmetz 2009). Since these mechanisms may also operate in globular clusters and in dwarf galaxies, high-velocity stars originating from these objects have also been proposed (Gualandris & Portegies Zwart 2007; Erkal et al. 2019; Fragione & Gualandris 2019).

Depending on the parameters and configurations, some of these mechanisms are capable of producing stars with velocities exceeding the escape velocity of the Galaxy, i.e. unbound stars. Currently, ∼20 stars with velocities exceeding the escape velocity of the Milky Way are confirmed. Unbound stars that result from the Hills mechanism are usually referred to as hypervelocity stars (HVS). With the exception of the S5-HVS1 (Koposov et al. 2020), which is an A-type star, all the confirmed unbound stars are B-type stars located in the distant Galactic halo. This is mainly a consequence of a survey bias, that searched for unexpected B-type stars in the halo (see Brown 2015, and references therein).

Recently, using astrometric data from *Gaia*, a large number of high-velocity stars in the solar neighbourhood have been reported (Hattori et al. 2018; Marchetti, Rossi & Brown 2019; Li et al. 2021), and some of them with a chance of being unbound stars. However, based on the chemical information provided by high-resolution spectra, it has been shown that most of these candidates follow a chemical pattern expected for the halo stars and would be

★ E-mail: fredifqh@gmail.com

© 2023 The Author(s)
Published by Oxford University Press on behalf of Royal Astronomical Society

Downloaded from https://academic.oup.com/mnras/article/522/3/3898/7143802 by SBD-FFLCH-USP user on 21 August 2023

likely bound to the Galaxy (Hawkins & Wyse 2018; Quispe-Huaynasi et al. 2022; Reggiani et al. 2022).

Abundances play an important role in placing constraints on the local of origin of the high-velocity stars through the concept of chemical tagging (Freeman & Bland-Hawthorn 2002). However, high-resolution spectra that might provide such abundances are not available for most of the high-velocity stars. On the other hand, during the last decade, photometric surveys such as SkyMapper (Keller et al. 2007), Pristine (Starkenburg et al. 2017), J-PLUS (Cenarro et al. 2019), S-PLUS (Mendes de Oliveira et al. 2019), miniJPAS (Bonoli et al. 2021), among others, have been used to search for potentially interesting astronomical objects for subsequent spectroscopic follow-up. These surveys collect data in multiple photometric bands strategically placed in regions sensitive to emission or absorption lines in the spectrum. Besides, photometry in multiple bands allows to obtain stellar parameters (Allende Prieto 2016, and references therein), providing a first insight into the properties of specific objects or populations.

In this work, we use the 12-band photometric information provided by the Javalambre Photometric Local Universe Survey (J-PLUS)[1] to characterize a sample of high-velocity stars through their stellar parameters, aiming to understand their possible origins. These stars have Galactocentric velocities higher than 400 km s^{-1} computed according to the astrometric parameters provided by *Gaia* DR3. In Section 2, we describe the data set considered for our analysis. In Section 3, we explain our selection strategy of high-velocity stars. We describe a kinematic study of this stellar sample in Section 4. Determination of stellar parameters based on spectral energy distributions (SED) and neural networks are presented in Section 5. Finally, Section 6 is devoted to conclusions.

2 DATA SOURCES

We use the photometry from the J-PLUS Data Release 2 (DR2) to infer effective temperature, $T_{\rm eff}$, surface gravity, log g, and metallicity, [Fe/H], of a sample of high-velocity stars observed by this survey. The parameters are inferred by applying, on one hand, a Convolutional Neural Network machine learning algorithm, hereafter CNN, and, on the other hand, a SED χ^2 fit.

J-PLUS is being conducted from the Observatorio Astrofísico de Javalambre (OAJ, Teruel, Spain; Cenarro et al. 2014) using the 83 cm Javalambre Auxiliary Survey Telescope (JAST80) and the T80Cam, a panoramic camera of 9.2 k × 9.2 k pixels that provides a 2 deg^2 field of view (FoV) with a pixel scale of 0.55 arsec pix^{-1} (Marín-Franch et al. 2015).

The J-PLUS filter system comprises the 12 photometric bands listed in Table 1. Four of these filters (g, r, i, z) are similar to the Sloan Digital Sky Survey (SDSS) broad-band filters, other six filters (u, J0395, J0410, J0430, J0515, J0861) are intermediate-band filters, and the last two (J0378, J0660) are narrow-band filters. This set of filters was strategically selected according to key spectral regions, to get a reliable SED for stars in our Galaxy and nearby galaxies.

The J-PLUS observational strategy, image reduction, and main scientific goals are presented in Cenarro et al. (2019). The J-PLUS DR2 comprises 1088 pointings (2176 deg^2) observed, reduced, and calibrated in all survey bands. The data are publicly available at the J-PLUS website.[2]

Table 1. J-PLUS photometric bands.

Filter	Central wavelength (nm)	FWHM (nm)	Spectral features
u	348.5	50.8	Balmer-break region
J0378	378.5	16.8	OII
J0395	395.0	10.0	Ca H + K
J0410	410.0	20.0	H_δ
J0430	430.0	20.0	*G* band
g	480.3	140.9	SDSS
J0515	515.0	20.0	Mg *b* triplet
r	625.4	138.8	SDSS
J0660	660.0	14.5	H_α
i	766.8	153.5	SDSS
J0861	861.0	40.0	Ca triplet
z	911.4	140.9	SDSS

To train and test our CNN algorithm, we use data from the Large Sky Area Multiobject Fiber Spectroscopic Telescope (LAMOST, Cui et al. 2012).[3] Specifically, we use the LAMOST Data Release 7 Low Resolution Spectra (DR7 LRS) Stellar Parameter Catalog of A, F, G, and K Stars, which provides spectra with resolution of $R = 1800$. Also, in order to test the CNN algorithm with an external catalogue, we used data from the Apache Point Observatory Galactic Evolution Experiment Data Release 17 (APOGEE DR17, Abdurro'uf et al. 2022)[4] for the stars in common with the J-PLUS DR2.

Finally, to assess the kinematic properties of the high-velocity stars, we use the data from the *Gaia* Data Release 3 (DR3). Unlike the previous releases of this survey, *Gaia* DR3 provides a lot of new data products, in particular, precise astrometric and photometric data for ∼1.8 billions of objects, and radial velocity information for ∼33 million stars (more information can be found in Gaia Collaboration 2022).

Along the text, we identify the stars using their *Gaia* ID rather than their J-PLUS ID, because this makes easier to cross-match the data with other surveys, including J-PLUS.

3 HIGH-VELOCITY STARS SELECTION

High-velocity stars can be primarily selected according to high radial velocities, high proper motions, or high tangential velocities. Here, however, we compute the actual Galactocentric velocity using the full information in the phase space given by the *Gaia* DR3 data and considering the photogeometric distances from Bailer-Jones et al. (2021).

The transformation from International Celestial Reference System (ICRS) coordinates to the Galactocentric reference frame (GRF) is performed using the PYIA package (Price-Whelan 2018). The parameters of the transformation are the ones set by default in version 4.0 of the ASTROPY Galactocentric frame: Sun's distance to the Galactic centre 8.122 kpc (Gravity Collaboration 2018), Sun's height over the Galactic mid-plane 20.8 pc (Bennett & Bovy 2019), and Sun's Cartesian velocity around the Galactic centre (12.9, 245.6, 7.78) km s^{-1} (Drimmel & Poggio 2018). The uncertainty propagation of the transformation is performed using 1000 Monte Carlo realizations, selected from multivariate normal distributions $\mathcal{N}(\boldsymbol{\theta}, \Sigma)$, where $\boldsymbol{\theta} = (\alpha, \delta, \varpi, \mu_\alpha, \mu_\delta, v_{\rm rad})$ are the

[1] https://www.j-plus.es/.
[2] https://www.j-plus.es/datareleases/data_release_dr2.
[3] http://www.lamost.org/public/.
[4] https://www.sdss4.org/dr17/.

Downloaded from https://academic.oup.com/mnras/article/522/3/3898/7143802 by SBD-FFLCH-USP user on 21 August 2023

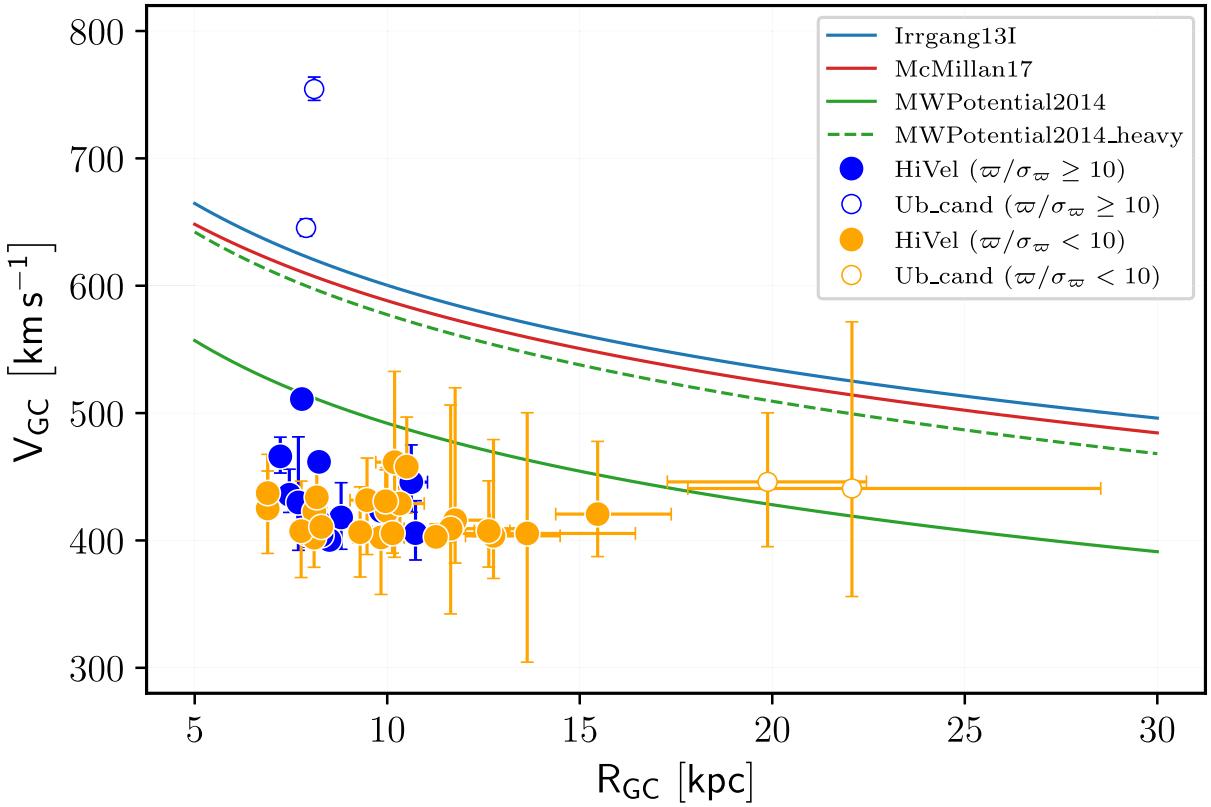

Figure 1. Galactocentric velocity as a function of Galactocentric distance. Blue dots are stars with $\varpi/\sigma_\varpi \geq 10$ and orange dots are stars with $\varpi/\sigma_\varpi < 10$. Open dots are stars that exceed at least one of the escape velocity curves (see text for details).

observables, and Σ is the covariance matrix provided by *Gaia*[5] Finally, we consider the median and the 16th and 84th percentiles over the distributions to get the final positions and velocities in the GRF.

We select stars with total GRF velocity exceeding 400 km s^{-1}. We consider this limit in order to avoid the high velocity component of the stellar velocity distribution of the Galactic disk stars. In this selection process, we only consider stars flagged with the following labels in *Gaia* DR3: positive parallax ($\varpi > 0$); apparent magnitude in the g band `phot_g_mean_mag` > 13; `ruwe` < 1.4; and $-3 <$ `astrometric_gof_al` < 3. The last two cuts ensure good astrometric solutions and avoids binary systems. We also impose `norm_dg` < -3, as recommended in Rybizki et al. (2021), to avoid stars with potential colour contamination from nearby sources.[6] We also consider stars with `grvs_mag-phot_g_mean_mag >-3` to avoid contamination from nearby bright sources that may affect radial velocity measurements in *Gaia* DR3 (Babusiaux et al. 2022).

Having selected the *Gaia* DR3 stars with high velocities, we cross-match that sample with the whole J-PLUS DR2 catalogue, and we end up with a set of 43 stars in common between them. Fig. 1 shows the Galactocentric velocity V_{GC} as a function of the Galactocentric distance R_{GC}. The solid lines in blue, red, and green in the figure represent the escape velocity curves calculated using the model I potential described in Irrgang et al. (2013), the McMillan potential (McMillan 2017), and the MWPotential2014 potential (Bovy 2015), respectively. The green dashed line is the escape velocity curve assuming a higher mass of 1.5×10^{11} M$_\odot$ for the halo in the MWPotential2014 potential (MWPotential2014_heavy), since its default value is underestimated compared to more recent estimates given in the literature (Bland-Hawthorn & Gerhard 2016).

The blue dots in Fig. 1 are stars with $\varpi/\sigma_\varpi \geq 10$ ($f = \sigma_\varpi/\varpi \leq 0.1$), orange dots are stars with $\varpi/\sigma_\varpi < 10$ ($f > 0.1$), and empty dots represent stars with median V_{GC} that exceed at least one of the escape velocity curves. With the exception of the stars *Gaia* DR3 1451 976 542 670 188 160 and *Gaia* DR3 2116 975 125 205 826 304 (open blue dots), all the other stars are bound to the potentials used (taking into account that the halo mass for the MWPotential2014 is underestimated). Looking at the astrometric parameters, we verify that the contribution to the high Galactocentric velocity of the two unbound stars comes from the corresponding radial velocities of 605 and 407 km s^{-1}, respectively. As high radial velocities in *Gaia* DR3 can be spurious measurements due to of very low signal to noise ratio (SNR), as explained in Katz et al. (2022), we check that 29 stars in our sample have SNR > 5 and 14 stars have SNR < 5. Actually, the SNR value for one of the unbound stars, *Gaia* DR3 1451 976 542 670 188 160, is very low (SNR = 2.7), and there is a high chance of its radial velocity being spurious. Unfortunately, this star has no spectrum available in the literature and there is no way to obtain a better estimate of its radial velocity at this moment.

In view of the above, we adopt a cut-off threshold of SNR ≥ 5, and reduce the sample to only 29 stars, thus excluding one of the two

[5]The elements of this matrix are the product of the uncertainties of two observables and their corresponding correlation coefficient. The correlation coefficients between v_{rad} and the other observables is assumed to be null, because they were obtained with different instruments.

[6]Originally, this flag was included in the external table `gedr3spur.main`, hosted at the German Astrophysical Virtual Observatory (GAVO), but now it is also available in the table `external.gaiaedr3_spurious` at https://gea.esac.esa.int/archive/.

Downloaded from https://academic.oup.com/mnras/article/522/3/3898/7143802 by SBD-FFLCH-USP user on 21 August 2023

Table 2. Astrometric parameters from *Gaia* DR3. The last column reports the radial velocity from spectroscopic surveys.

Gaia DR3 ID	α (deg ± mas)	δ (deg ± mas)	ϖ (mas)	μ_α (mas yr^{-1})	μ_δ (mas yr^{-1})	$v_{\rm rad}$ (*Gaia*) (km s^{-1})	$v_{\rm rad}$ (Spec) (km s^{-1})
367 292 825 627 187 328	12.08 ± 0.01	37.37 ± 0.01	0.10 ± 0.02	20.21 ± 0.02	− 5.76 ± 0.01	− 17.81 ± 4.17	− 11.47 ± 0.90 [c]
1336 662 924 245 986 176	260.49 ± 0.01	35.65 ± 0.01	0.11 ± 0.01	− 11.46 ± 0.01	− 1.74 ± 0.02	− 508.56 ± 4.43	
1342 335 888 849 476 864	265.21 ± 0.01	37.65 ± 0.01	0.26 ± 0.01	− 19.09 ± 0.01	18.25 ± 0.01	− 91.75 ± 4.04	
1343 323 971 845 379 968	262.89 ± 0.01	38.24 ± 0.01	0.05 ± 0.01	− 3.81 ± 0.02	− 8.19 ± 0.02	− 268.35 ± 5.50	− 273.48 ± 3.85 [b]
139 563 911 305 1405 824	230.92 ± 0.01	45.84 ± 0.01	0.18 ± 0.01	− 25.17 ± 0.01	− 8.28 ± 0.01	− 115.86 ± 2.65	− 123.93 ± 0.62 [c]
1396 963 57 7886 583 296	237.73 ± 0.01	44.44 ± 0.01	0.01 ± 0.01	− 1.61 ± 0.01	− 4.92 ± 0.01	− 413.78 ± 0.79	− 419.55 ± 1.32 [c]
1399 596 186 680 287 616	238.68 ± 0.01	47.56 ± 0.01	0.05 ± 0.01	− 8.50 ± 0.01	2.22 ± 0.02	17.38 ± 3.44	
1428 946 275 194 761 216	243.21 ± 0.01	54.12 ± 0.01	0.65 ± 0.01	15.54 ± 0.01	13.69 ± 0.02	80.97 ± 2.88	80.92 ± 4.13 [b]
1565 897 801 417 595 136	202.12 ± 0.01	57.53 ± 0.01	0.13 ± 0.02	− 4.06 ± 0.02	− 9.46 ± 0.02	257.19 ± 4.59	249.83 ± 3.55 [b]
1613 154 433 222 682 368	225.84 ± 0.01	57.03 ± 0.01	0.71 ± 0.01	− 66.76 ± 0.01	− 29.97 ± 0.02	− 446.42 ± 5.30	
1774 483 437 903 554 944	332.25 ± 0.02	15.25 ± 0.02	0.64 ± 0.02	− 47.84 ± 0.02	− 29.08 ± 0.02	− 280.38 ± 5.69	− 276.83 ± 3.70 [b]
1890 506 653 647 184 768	341.80 ± 0.01	32.48 ± 0.01	0.17 ± 0.01	− 8.34 ± 0.01	− 10.60 ± 0.01	46.32 ± 0.99	42.57 ± 3.75 [b]
1901 537 847 650 215 424	338.95 ± 0.01	33.41 ± 0.02	0.14 ± 0.02	14.49 ± 0.02	− 11.04 ± 0.02	− 21.84 ± 2.52	
2092 453 885 607 135 744	284.18 ± 0.01	35.19 ± 0.01	0.07 ± 0.01	− 3.41 ± 0.01	− 8.88 ± 0.01	− 415.92 ± 4.02	
2104 759 069 985 260 416	282.33 ± 0.01	42.41 ± 0.01	0.07 ± 0.01	5.29 ± 0.02	− 5.83 ± 0.02	− 419.57 ± 3.76	
2116 975 125 205 826 304*	279.92 ± 0.01	42.76 ± 0.01	1.02 ± 0.01	7.06 ± 0.01	− 13.40 ± 0.02	407.77 ± 7.32	− 6.91 ± 3.14 [b]
2117 018 933 872 374 272	280.05 ± 0.01	43.32 ± 0.01	0.00 ± 0.01	− 2.36 ± 0.01	− 3.68 ± 0.01	− 406.48 ± 1.14	− 405.98 ± 0.00 [a, b]
2117 987 431 816 799 104	278.49 ± 0.01	44.76 ± 0.01	0.08 ± 0.01	1.36 ± 0.02	− 8.11 ± 0.02	− 454.03 ± 2.97	
2118 955 689 244 636 672	282.04 ± 0.01	45.42 ± 0.01	0.11 ± 0.01	− 1.56 ± 0.01	− 12.09 ± 0.02	− 51.18 ± 2.86	
2154 188 852 160 448 512	279.26 ± 0.01	57.51 ± 0.01	0.11 ± 0.01	7.94 ± 0.01	− 6.22 ± 0.01	− 129.53 ± 1.94	
2155 887 803 783 818 624	284.46 ± 0.01	60.12 ± 0.01	0.05 ± 0.01	4.68 ± 0.01	− 2.59 ± 0.01	− 241.15 ± 1.94	− 249.08 ± 0.92 [c]
2266 761 044 499 471 488	272.99 ± 0.01	72.30 ± 0.01	0.16 ± 0.01	3.88 ± 0.02	15.07 ± 0.02	− 115.46 ± 4.57	
2577 104 317 472 212 736	18.53 ± 0.02	7.86 ± 0.01	0.12 ± 0.02	15.07 ± 0.02	− 1.30 ± 0.02	73.14 ± 3.40	51.67 ± 6.36 [b]
4570 724 026 270 780 416	261.51 ± 0.01	25.69 ± 0.01	0.11 ± 0.02	− 5.35 ± 0.01	− 17.46 ± 0.02	− 159.47 ± 4.29	
4574 589 702 994 326 144	257.40 ± 0.01	26.60 ± 0.01	0.13 ± 0.02	− 0.12 ± 0.01	9.12 ± 0.01	− 343.03 ± 2.98	
4601 980 530 506 725 888	262.94 ± 0.01	32.99 ± 0.01	0.30 ± 0.01	− 2.63 ± 0.01	− 35.06 ± 0.01	− 412.51 ± 3.18	− 411.93 ± 5.32 [b]
4603 065 267 448 558 848	268.90 ± 0.01	31.68 ± 0.01	0.03 ± 0.01	− 3.55 ± 0.01	− 5.79 ± 0.01	− 366.20 ± 2.45	
4609 671 373 825 731 584	270.19 ± 0.01	37.31 ± 0.01	0.11 ± 0.01	7.05 ± 0.02	− 0.18 ± 0.02	− 420.53 ± 5.10	
4610 093 483 212 194 304	270.88 ± 0.01	38.05 ± 0.01	0.17 ± 0.01	− 19.75 ± 0.02	3.37 ± 0.02	− 410.08 ± 4.93	

Notes. * Excluded from the final sample due to discrepant radial velocities; possible eclipsing binary (Heinze et al. 2018).
[a] APOGEE DR17.
[b] LAMOST DR7 Low-resolution spectra.
[c] LAMOST DR7 Medium-resolution spectra.

unbound candidates. The astrometric parameters of these 29 stars from *Gaia* DR3 are reported in Table 2. A similar SNR cut-off has been adopted in Marchetti, Evans & Rossi (2022), however, it is not a well-defined threshold and some stars may still have spurious radial velocities even with a higher SNR. In order to check this, we search for radial velocity information in the spectroscopic surveys described in Section 2, and we find 12 stars in the LAMOST DR7 and 1 additional star which is in both the LAMOST DR7 and the APOGEE DR17. These radial velocities are also reported in Table 2. Comparing them with the ones provided by *Gaia* DR3, and excluding one star which shows very discrepant values, we find that the mean differences are $\sim 4 \pm 6$ km s^{-1}, showing a good agreement between the radial velocities from the different sources.

The aforementioned discrepant radial velocity values correspond to star *Gaia* DR3 2116 975 125 205 826 304, which is the other unbound candidate in our sample. This star has been reported as an eclipsing binary candidate by Heinze et al. (2018), which may be the reason for the discrepancy. The LAMOST radial velocity for this star has been estimated from a spectrum with lower resolution but higher SNR than that of *Gaia*. Thus, in principle, we cannot decide whether one estimate is better than the other. We decide to exclude this star from our sample, since it might not even exceed the 400 km s^{-1} velocity limit, although it would deserve a dedicated analysis through high-resolution spectroscopy to better assess its radial velocity.

After all the above considerations, our final sample is composed of 28 stars, all bounded to the Galaxy. From here in after, we will refer to this as the HiVel sample.

4 KINEMATICS AND DYNAMICS

4.1 Kinematical spaces

Fig. 2 shows three different spaces used to characterize the stars based on their kinematical properties. The orbital energy, E, angular momentum, L_z, and actions, J_r, J_ϕ, J_z, have been calculated using GALPY (Bovy 2015).[7]

The first kinematical space is the Toomre diagram, shown in the upper panel of Fig. 2. This diagram using only velocity information allows to separate the disk stellar population (represented by the shaded region in the plot) from the halo stellar population, without having to assume any gravitational potential for the Galaxy. This is possible because a significant contribution is expected to the radial and vertical components of the velocity of the halo stars. However, the limit between these populations is not well defined. According to this diagram, most stars in the HiVel sample display a kinematic behaviour typical of halo stars. In addition, the negative azimuthal component of the velocity indicate that some stars in the sample have retrograde motion.

The second kinematical space is the energy versus angular momentum diagram, shown in the left bottom panel of Fig. 2, also known as Lindblad diagram. At variance with the Toomre diagram, the Lindblad diagram requires to assume a gravitational potential for the Galaxy. In particular, the two quantities E, L_z are constants in

[7] https://docs.galpy.org.

Downloaded from https://academic.oup.com/mnras/article/522/3/3898/7143802 by SBD-FFLCH-USP user on 21 August 2023

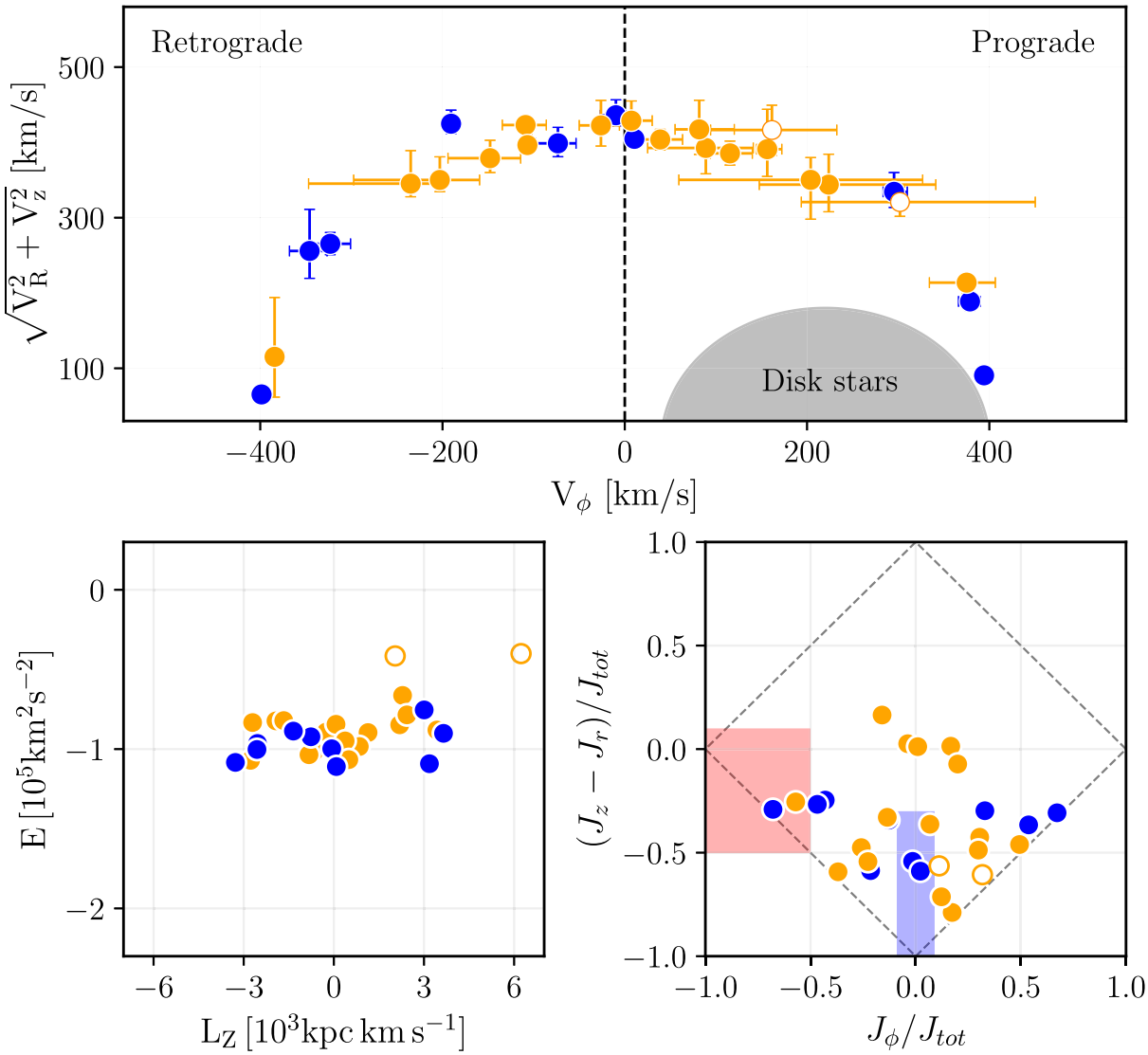

Figure 2. Toomre diagram (top), Lindblad diagram (left bottom), and scaled actions diamond diagram (right bottom). The shaded region in the Toomre diagram is the approximate locus of the disk stars. The areas in blue and magenta in the actions diamond correspond to the *Gaia*-Enceladus/Sausage and the Sequoia mergers remnants, respectively. Colour code is the same as in Fig. 1.

axisymmetric potentials. This diagram also allows to separate the disk from the halo stars (Lane, Bovy & Mackereth 2022), due to the fact that disk stars have positive angular momentum and moderate orbital energy. In our case, we verify that the HiVel stars are bound to the galaxy ($E < 0$) and, as in the Toomre diagram, some of them display prograde motion ($L_z > 0$) while others have retrograde motion ($L_z < 0$).

The Lindblad kinematic space has been applied, for example, to identify the Helmi stellar stream (Helmi et al. 1999), and it is now widely used to identify structures in the Galactic halo (Helmi 2020). The regions occupied by these halo structures in the Lindblad diagram are not well defined, and some of them may overlap (see Naidu et al. 2020; Bonaca et al. 2021). Assuming that our HiVel sample, at least partially, belongs to the set of accreted stars in these structures, it represents an extreme component, both in terms of orbital energy and angular momentum. The only two halo structures that include such extreme components are the Sequoia structure, which has stars with retrograde motion, and the *Gaia*-Enceladus/Sausage structure, which has stars with high angular momentum (Myeong et al. 2019). This does not rule out the possibility of the HiVel stars to belong to other structures, but the two mentioned above appear as the most probable. At the limit of high orbital energies, there is no separation between the *Gaia*-Enceladus/Sausage and Sequoia, since the *Gaia*-Enceladus/Sausage has a sub-population of star with retrograde motion. In principle, only a detailed analysis of the chemical abundances may help to segregate these two structures, although this is still an open problem (Aguado et al. 2021; Horta et al. 2023).

The third kinematical space is the actions diagram, shown in the right bottom panel of Fig. 2, also known as the actions diamond space due to its shape (represented by the dashed lines). The actions J_r, J_ϕ, and J_z are integrals of motion of the system. In axisymmetric potentials, in particular, $J_\phi = L_z$, but J_r and J_z are not well defined. The actions for our HiVel stars have been calculated using the Stäckel approximation (Binney 2012). This diagram allows to segregate stellar populations (Lane et al. 2022), and to identify substructures in the Galactic halo (Myeong et al. 2019; Naidu et al. 2020). Stars with eccentric orbits tend to group in the lower corner of the diamond, while

Downloaded from https://academic.oup.com/mnras/article/522/3/3898/7143802 by SBD-FFLCH-USP user on 21 August 2023

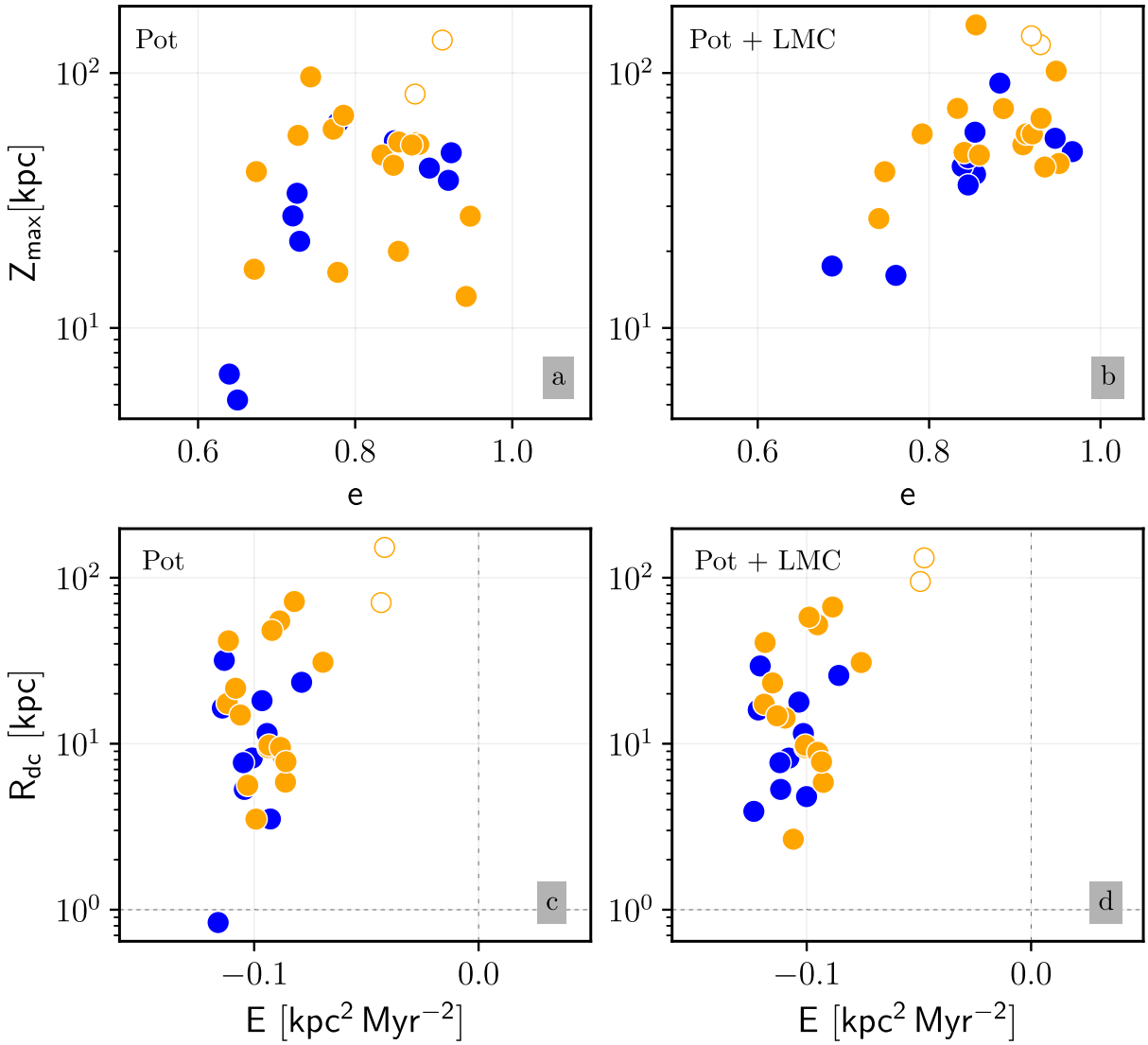

Figure 3. *Top:* Maximum height above the Galactic plane as a function of orbital eccentricity. *Bottom:* Galactocentric distance during the last crossing through the Galactic disk (R_{dc}) as a function of orbital energy. The vertical lines show the limit between bound and unbound stars and the horizontal lines correspond to 1 kpc. Panels a and c show the results without the LMC, while panels b and d consider the LMC. Colour code is the same as in Fig. 1.

stars with retrograde and prograde motions concentrate in the left and right corners, respectively. The region in magenta in this diagram corresponds to the location of the remnants of the Sequoia merger, with highly retrograde stars, and the region in blue corresponds to the location of the remnants of the *Gaia*-Enceladus/Sausage merger, with stars in highly eccentric orbits (Myeong et al. 2019). The limits of these regions are not well defined and we adopt the ones given in Monty et al. (2020). We can see that some stars of the HiVel sample lie within or very close to these two regions.

Confirming the association of the HiVel stars to these halo structures might provide support for the mechanism proposed by Abadi et al. (2009) to generate high velocity stars, i.e. stellar streams formed by galactic tidal forces acting during the passage of dwarf satellite galaxies through the perigalactic. Tidal disruption processes can also involve globular clusters, providing an additional mechanism to generate high velocity stars (Capuzzo-Dolcetta & Fragione 2015). Chemical information is mandatory to support this scenario, since globular cluster stars are expected to display an anticorrelation between aluminium and magnesium (Bastian & Lardo 2018).

4.2 Orbital evolution

In order to obtain the orbital parameters of the HiVel stars, and to try to constrain their origins, we use the current positions and velocities in the GRF to perform a back-in-time orbit integration over 10 Gyr. In these simulations, we adopt the Irrgang model I potential (Irrgang et al. 2013), which is an updated version of the Allen & Santillan (1991) potential. We also include the gravitational potential associated to the Large Magellanic Cloud (LMC), the most massive satellite of the Milky Way, modelled by a Hernquist potential with a scale radius of 17.13 kpc (Boubert, Erkal & Gualandris 2020) and a mass of 1.8×10^{11} $M_\odot$ (Shipp et al. 2021). Dynamical friction or mass loss acting on the LMC are not considered. The integration is performed using the GALPY routines and the output is registered every 1 Myr. The average orbital parameters and their associated uncertainties are then computed from 1000 orbit realizations for each star, and the initial conditions for each realization is taken within the 1σ uncertainties of the corresponding GRF positions and velocities.

Fig. 3a and b display the maximum height relative to the Galactic plane, Z_{max}, as a function of the orbital eccentricity, e, with and

Downloaded from https://academic.oup.com/mnras/article/522/3/3898/7143802 by SBD-FFLCH-USP user on 21 August 2023

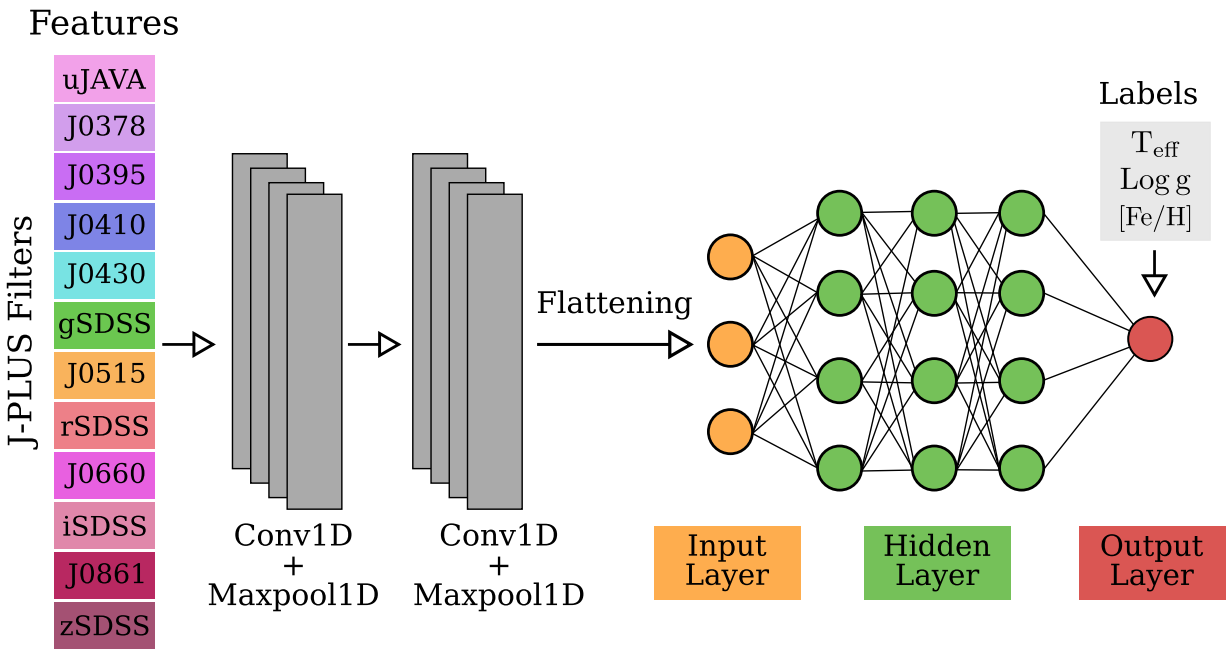

Figure 4. Configuration of the CNN architecture used to infer the stellar parameters.

without the LMC perturbation. We note that all the stars are in very eccentric Galactocentric orbits, $e > 0.6$, and they become even more eccentric when the LMC is included. We also note that, in general, $Z_{\rm max}$ is large, and becomes >10 kpc for all the stars when the LMC is included.

Fig 3c and d display the Galactocentric distance during the last Galactic disc crossing of the star, $R_{\rm dc}$ as a function of the orbital energy. This parameter may be used as an indicative for the Hills mechanism as a possible origin of the high velocities. Panel **c** shows that one of the stars passes at $R_{\rm dc} < 1$ kpc, with a chance of having its origin in the Galactic centre, however, this chance is excluded when the perturbation of the LMC is taken into account.

We also check whether the high velocity stars may originate in the LMC. We monitor the number of times that each star has a close encounter with the LMC during the last 10 Gyr. A close encounter is assumed to occur when the star passes at a distance of <5 kpc from the LMC. Then, the probability of a star to originate in the LMC is computed as the fraction of orbits that had a close encounter over the 1000 realizations[8] of the star orbit. Most of the stars have a very low probability (<2%), and only one star (*Gaia* DR3 2155 887 803 783 818 624) have a slightly higher probability of only ∼10%.

5 STELLAR PARAMETERS

In order to assess the stellar properties of the HiVel stars, we apply two different techniques: (i) a CNN machine learning algorithm, and (ii) a SED fit using the photometry of J-PLUS DR2 together with the Virtual Observatory SED Analyzer (VOSA, Bayo et al. 2008).[9]

5.1 Parameters determined by the CNN

At variance with previous works that applied machine learning algorithms to determine stellar parameters from J-PLUS data (Whitten et al. 2019; Galarza et al. 2022; Yang et al. 2022), we apply here a CNN architecture. CNNs have been previously used for the determination of stellar parameters from spectroscopic data and more details on this can be found in Gebran et al. (2022, and references therein). We prefer this architecture because it is easy to implement through KERAS (Chollet et al. 2015), it is applicable to one dimensional sequential data, and it allows for single or multiple outputs regression.

As illustrated in Fig. 4, the features of the CNN (input data) are the 12 magnitudes provided by the J-PLUS photometric filters, corrected by dust extinction (unredden) using the 2D SFD dust map (Schlafly & Finkbeiner 2011) and the DUSTMAPS Python package (Green 2018).[10] The extinction coefficients for J-PLUS bands are extracted from table 1 of López-Sanjuan et al. (2021). Since the order of the features is important in the CNN architecture for pattern recognition, we order the magnitudes according to increasing wavelength. The labels of the data (output parameters) are the values of $T_{\rm eff}$, [Fe/H] and log g.

The data used for training and testing are built from the cross-match of data between J-PLUS DR2, *Gaia* DR3 and LAMOST DR7. In order to use a reliable sample, we perform the following quality cuts:

(i) For J-PLUS data, we consider sources with: 95 per cent of chance of being a star (`class_star` > 0.95), as given by SEXTRACTOR, apparent magnitudes `mag_auto` < 18 in all the photometric bands, and uncertainties in magnitudes `mag_err_auto` < 0.15.

(ii) For *Gaia* data, we consider sources with positive parallax, `ruwe` < 1.4, `norm_dg` < −3, and `fidelity_v2` > 0.5.

(iii) For LAMOST data, we consider stars with $3800 \leq T_{\rm eff} \leq 8000$ K, with uncertainties <100 K, and also uncertainties <0.1 in log g and <0.3 dex in [Fe/H].

With such quality cuts, we obtain a sample of ∼120 000 stars, of which 80 per cent is used for training and 20 per cent for testing.

The initial CNN architecture for training the algorithm is illustrated in Fig. 4. We use two one-dimensional convolutional layers

[8]Within the orbit uncertainties.
[9]http://svo2.cab.inta-csic.es/theory/vosa/.
[10]https://dustmaps.readthedocs.io.

Downloaded from https://academic.oup.com/mnras/article/522/3/3898/7143802 by SBD-FFLCH-USP user on 21 August 2023

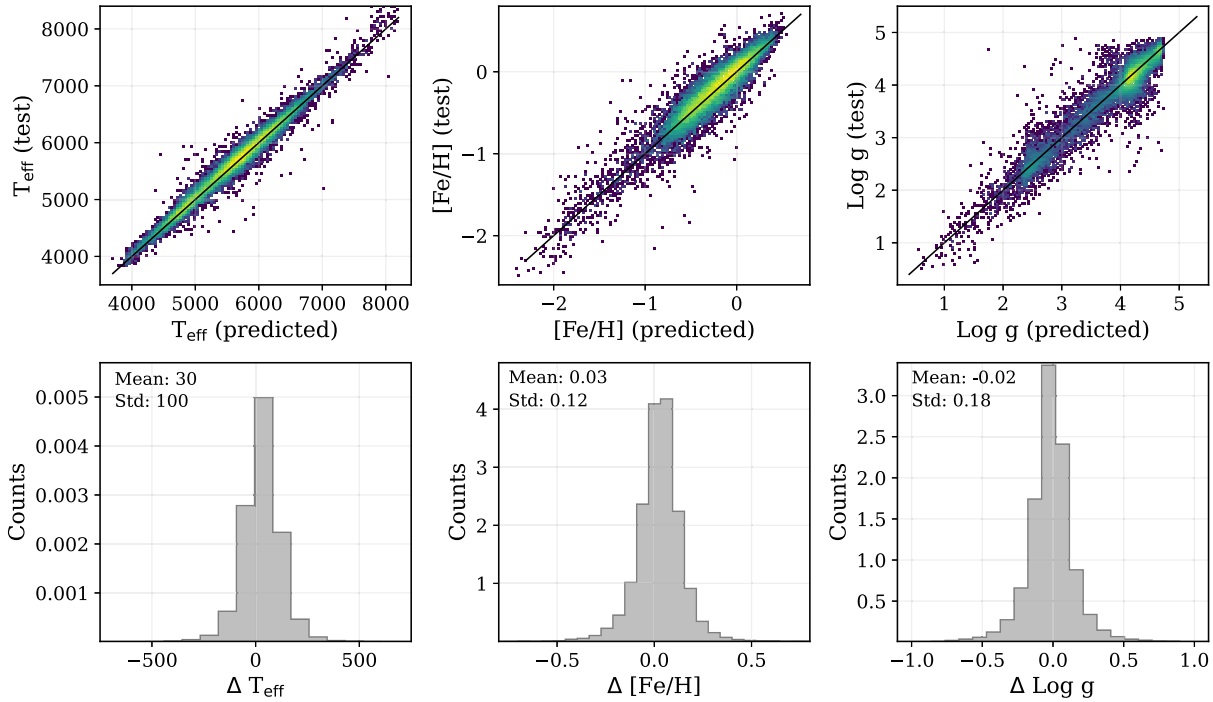

Figure 5. Test results of the CNN model. The upper panels compare the stellar parameters predicted by the model to those given in the LAMOST catalogue. The colour scale represents the density of points. The lower panels show the histograms of the differences LAMOST − CNN for the test sample.

(Conv1D) to build the features map from the input data. A one-dimensional maxpooling layer (Maxpool1D) is associated to each of the Conv1D. The Maxpool1D layers are used to reduce the number of inputs that will feed the neural network. The network itself is composed of an input layer, three hidden layers, and an output layer. The Relu activation function is used in both the Conv1D layers and the network layers. We select the Adam optimization algorithm (Kingma & Ba 2015), and the mean absolute error (mae) loss function.

The final hyperparameters of the CNN, learning rate, number of kernels, kernel size, and number of neurons in each hidden layer are obtained via the KERAS TUNER (O'Malley et al. 2019), using the Bayesian search optimizer.

5.1.1 Model testing

The horizontal axes in the upper panels of Fig. 5 show the values of $T_{\rm eff}$, [Fe/H] and log g predicted by the CNN for the test sample, while the vertical axes show the corresponding values provided by the LAMOST catalogue, also for the test sample. The lower panels in Fig. 5 show the histograms of the differences between the catalogue values and the predicted values (i.e. LAMOST − CNN). Overall, the stellar parameters show a good agreement. The mean values of the offsets are $T_{\rm eff} = 30$ K, [Fe/H] $= +0.03$ dex, and log $g = -0.02$, and the 1σ scatter is 100 K, 0.12 dex, and 0.18, respectively.

In addition, in order to test the CNN with an external catalogue, we apply the model for ∼8000 stars that are found in common between the JPLUS DR2 and the APOGEE DR17 catalogues. The comparison of the parameters given by the CNN and those given by APOGEE is illustrated in Fig. 6. In general, there is a good agreement between the parameters. However, for values of $T_{\rm eff}$ lower than ∼4500 K and higher than ∼6000 K, the offsets are considerable. For log g, there is also a considerable offset for values $\lesssim 2.0$, but for [Fe/H] the agreement is good over the whole range of metallicities. These offsets are expected since we use LAMOST data to train the model, and it is known that LAMOST has discrepancies with APOGEE due to systematic effects (a discussion on these discrepancies found in previous data releases is given in Anguiano et al. 2018).

Table 3 reports the values obtained by applying the VOSA model to our sample of HiVel stars.

5.2 Parameters determined by VOSA

In VOSA , the observed SED of a star obtained from the 12 photometric bands of J-PLUS DR2 is compared to several synthetic SEDs derived from a grid of stellar atmosphere models and properly convolved with the J-PLUS filters. The resulting stellar parameters are those of the synthetic SED that minimizes the χ^2 value of the comparison. It is worth noting that the input J-PLUS magnitudes in this analysis are already unredden, as explained in Section 5.1, and we do not let VOSA to perform the extinction (A_V) correction.

We consider two different grids of models. One grid is from Castelli & Kurucz (2003),[11] and considers: $T_{\rm eff}$ ranging from 3000 to 13 000 K in steps of 250 K; log g ranging from 0.0 to 5.0 in steps of 0.5; and [Fe/H] values of −2.5, −2.0, −1.5, −1.0, −0.5, 0.0, +0.2, and +0.5 dex.

The other grid is from Allard et al. (2011), calibrated using the abundances of Asplund et al. (2009), and considers: $T_{\rm eff}$ ranging from 3000 to 7000 K in steps of 100 K, and from 7000 to 12 000 K in steps of 200 K; log g ranging from −0.5 to 5.0 in steps of 0.5; and [Fe/H] values of −3.0, −2.5, −2.0, −1.5, −1.0, −0.5, 0.0, +0.3, and +0.5 dex.

[11] https://www.stsci.edu/hst/instrumentation/reference-data-for-calibration-and-tools/astronomical-catalogs/castelli-and-kurucz-atlas.

Downloaded from https://academic.oup.com/mnras/article/522/3/3898/7143802 by SBD-FFLCH-USP user on 21 August 2023

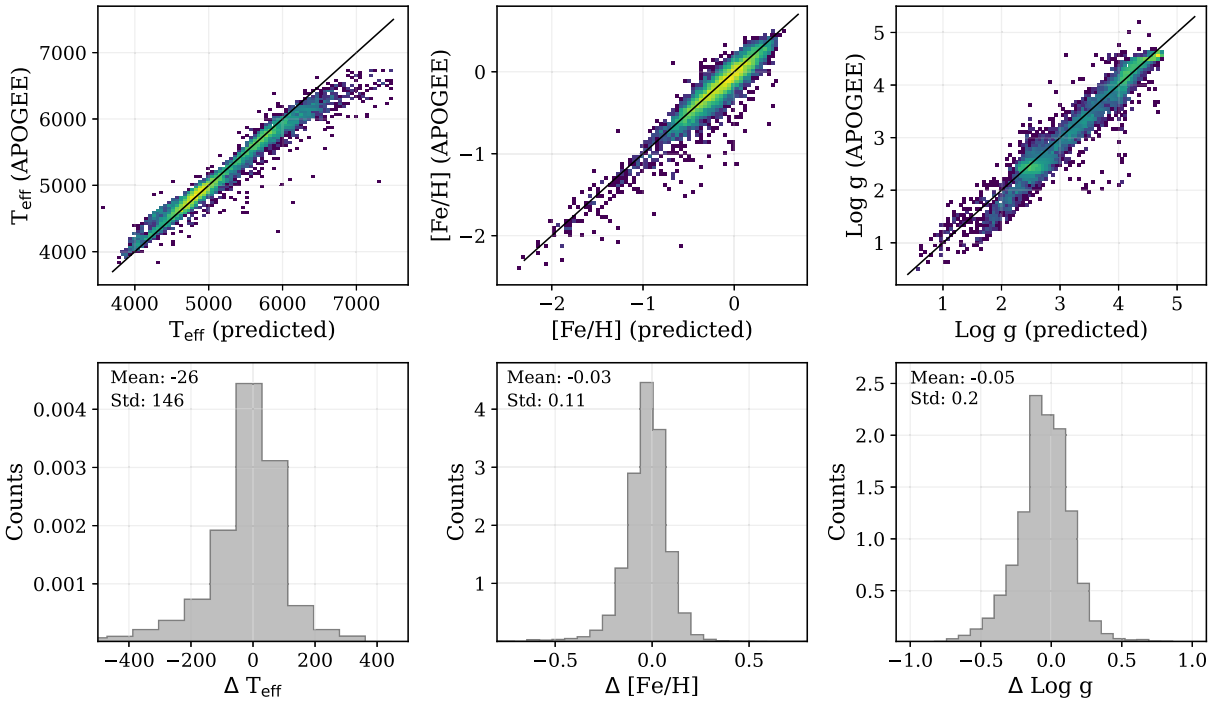

Figure 6. Application of the CNN model to the APOGEE DR17 data. The upper panels compare the stellar parameters predicted by the model to those given by APOGEE. The colour scale represents the density of points. The lower panels show the histograms of the differences APOGEE − CNN.

The best fit values of $T_{\rm eff}$ obtained by VOSA for our sample of HiVel stars, with each grid, are reported in Table 3. The uncertainty in this parameter corresponds to the step value in the model grids divided by two. According to the VOSA documentation,[12] the comparisons between the values of metallicity and surface gravity provided by VOSA and those given in the literature, in general, do not show a good agreement. This is due to the fact that the variations of these two parameters do not have a significant contribution to the shape of the SED, which results in degeneracies. Therefore, the values of [Fe/H] and log g given by VOSA are not expected to be reliable and are not reported in Table 3. VOSA was unable to determine the temperature of one star with the Kurucz models, probably because its actual metallicity is outside the limits of the grid.

5.3 Comparison between the CNN and VOSA

Fig. 7 illustrates the comparison of the effective temperature calculated for the HiVel sample using the CNN and VOSA with grid model Kurucz ODFNEW /NOVER, alpha: 0.4 (2003). There is a mean offset (CNN − VOSA) of 204 K, which reduces to 180 ± 171 K when excluding the star 367 292 825 627 187 328 that displays the largest offset (∼800 K). The large discrepancy in this star may be associated to the fact that it has been classified as a variable star (RR Lyrae) in the literature (Drake et al. 2013; Sesar et al. 2017). This star would deserve a more detailed study and therefore it will not be considered in the rest of our analysis. A similar result in obtained when comparing the CNN to VOSA with grid model BT-Settl (AGSS2009), with almost the same offset (169 ± 128 K). In order to verify if this offset in temperature is actually systematic, it would be necessary to consider a much larger sample of stars.

For completeness, we compare the values of [Fe/H] and log g, and we obtain mean offsets (CNN − VOSA) of +0.24 ± 0.43 dex and 0.24 ± 1.15, respectively, using the Kurucz model grid. Using the BT-Settl model grid, we observe less scatter but larger offsets: +0.31 ± 0.31 dex in [Fe/H] and 0.91 ± 0.59 in log g.

5.4 Comparison to other models

As mentioned in Section 5.1, other machine learning algorithms have been applied to J-PLUS data to determine stellar parameters. Here in particular, we compare the results of our CNN to the results obtained with the SPHINX neural network (Whitten et al. 2019) and the CSNET neural network (Yang et al. 2022).

The current model of SPHINX (Whitten et al. 2021) has been trained using the 12 filter photometry from the Southern Photometric Local Universe Survey (S-PLUS, Mendes de Oliveira et al. 2019),[13] which is a twin survey of J-PLUS but for the Southern Hemisphere. In particular, the model applied here is based on the magnitudes of S-PLUS internal Data Release 4 (iDR4), properly unredden. The training labels were taken from a combination of LAMOST DR7 and the Sloan Extension for Galactic Understanding and Exploration (SEGUE DR9, Yanny et al. 2009),[14] totalling ∼7000 stars. The network was trained for a range of 4000 ≤ $T_{\rm eff}$ ≤ 6750 K and −2.5 ≤ [Fe/H] ≤ 0.0. SPHINX only provides estimates for $T_{\rm eff}$ and [Fe/H].

The application of the current SPHINX model to our HiVel sample produces the results reported in Table 3. SPHINX was unable to provide estimates for two stars that are outside the temperature range of the training. In general, we observe a good correlation between the temperature and the metallicity determined by our CNN and SPHINX, although there is a systematic offset (CNN − SPHINX) of

[12] http://svo2.cab.inta-csic.es/theory/vosa/helpw4.php?otype=star&action=help&what=quality.

[13] https://www.splus.iag.usp.br/.

[14] https://www.sdss4.org/surveys/segue/.

Downloaded from https://academic.oup.com/mnras/article/522/3/3898/7143802 by SBD-FFLCH-USP user on 21 August 2023

Table 3. Stellar parameters derived from different models.

Gaia DR3 ID	CNN (this work)			VOSA w/CK03 [a]	VOSA w/A11 [b]	SPHINX (W21) [c]		CSNET (Y22) [d]		
	$T_{\rm eff}$ ±95 (K)	[Fe/H] ±0.1 (dex)	log g ±0.2	$T_{\rm eff}$ ±125 (K)	$T_{\rm eff}$ ±50 (K)	$T_{\rm eff}$ (K)	[Fe/H] dex	$T_{\rm eff}$ ±55 (K)	[Fe/H] ±0.07 (dex)	log g ±0.15
367 292 825 627 187 328*	7057	−0.8	4.2	6250	6400	–	–			
1336 662 924 245 986 176	4982	−2.0	2.1	5000	4900	5209 ± 21	−1.56 ± 0.13			
1342 335 888 849 476 864	5250	−1.5	2.6	5000	5100	5466 ± 15	−1.26 ± 0.43			
1343 323 971 845 379 968	5619	−1.3	2.8	5250	5200	5703 ± 7	−1.28 ± 0.61			
1395 639 113 051 405 824	5616	−1.3	2.9	5250	5300	5714 ± 30	−1.02 ± 0.38			
1396 963 577 886 583 296	3961	−1.0	0.7	4000	4000	–	–	4105	−0.80	1.51
1399 596 186 680 287 616	5013	−2.3	1.8	5000	4900	5023 ± 3	−2.26 ± 0.18	4701	−2.45	1.35
1428 946 275 194 761 216	5576	−0.5	3.8	5750	5600	5721 ± 10	−0.53 ± 0.17	5637	−0.47	3.86
1565 897 801 417 595 136	5918	−1.2	3.4	5500	5600	5959 ± 25	−1.73 ± 0.93	5696	−1.68	3.32
1613 154 433 222 682 368	6170	−1.5	4.2	6000	6100	6350 ± 7	−1.53 ± 0.33			
1774 483 437 903 554 944	5777	−1.6	3.8	5500	5500	5968 ± 2	−1.53 ± 0.57			
1890 506 653 647 184 768	4646	−0.2	2.4	4500	4500	4981 ± 79	−0.20 ± 0.27			
1901 537 847 650 215 424	4879	−1.1	2.4	4750	4700	5105 ± 24	−1.01 ± 0.19	4913	−1.13	2.50
2092 453 885 607 135 744	5004	−1.8	1.8	4750	4800	5131 ± 38	−0.86 ± 0.19			
2104 759 069 985 260 416	4837	−1.1	2.5	4500	4500	5040 ± 29	−0.85 ± 0.13			
2117 018 933 872 374 272	4464	−1.7	1.1	4500	4300	4521 ± 19	−0.97 ± 0.23			
2117 987 431 816 799 104	4928	−1.8	2.1	4900	4900	5095 ± 67	−1.60 ± 0.48			
2118 955 689 244 636 672	4978	−0.2	2.8	4750	4800	5160 ± 51	−0.19 ± 0.17			
2154 188 852 160 448 512	4826	−1.8	2.1	4750	4700	5019 ± 36	−1.36 ± 0.40			
2155 887 803 783 818 624	4702	−1.3	1.7	4500	4600	4869 ± 29	−1.16 ± 0.28			
2266 761 044 499 471 488	5760	−1.3	3.0	5250	5300	5881 ± 25	−1.89 ± 0.43			
2577 104 317 472 212 736	5020	−1.1	2.4	5000	4900	5282 ± 7	−0.74 ± 0.08	5131	−1.03	2.52
4570 724 026 270 780 416	5127	−1.1	2.5	4750	4900	5273 ± 21	−0.88 ± 0.09			
4574 589 702 994 326 144	4980	−1.2	2.4	4750	4900	5199 ± 23	−1.05 ± 0.06	4926	−1.17	2.53
4601 980 530 506 725 888	5275	−2.0	2.3	5250	5100	5516 ± 11	−1.58 ± 0.50			
4603 065 267 448 558 848	4928	−2.6	1.3	–	4700	4781 ± 77	−2.31 ± 0.11	4544	−2.01	1.61
4609 671 373 825 731 584	5185	−2.1	2.2	5000	5000	5372 ± 11	−1.99 ± 0.07			
4610 093 483 212 194 304	5053	−1.1	2.6	5100	5100	5260 ± 12	−1.06 ± 0.08			

Notes. * RR Lyrae variable star.
[a] Castelli & Kurucz (2003), model Kurucz ODFNEW /NOVER, alpha: 0.4 (2003).
[b] Allard, Homeier & Freytag (2011), model BT-Settl (AGSS2009).
[c] Whitten et al. (2021).
[d] Yang et al. (2022).

−157 ± 94 K in $T_{\rm eff}$ and −0.16 ± 0.31 dex in [Fe/H]. According to SPHINX, our HiVel stars would be slightly hotter and less metal-poor than estimated from our CNN. Such offset is likely related to differences in the unredden magnitudes between J-PLUS and S-PLUS.

The CSNET model, on the other hand, has been trained with J-PLUS DR1 data and its main advantage is that it provides not only the basic stellar parameters, but also the abundances of α-elements and other specific species. As we will see later (Section 5.6), α-elements abundance is relevant to determine the possible origin of the high velocity stars. Since CSNET was applied to DR1, the corresponding catalogue[15] contains only eight stars in common with our HiVel sample based on DR2. The corresponding stellar parameters of these eight stars are reported in Table 3. These results show a better agreement with our CNN, with mean offsets of 77 ± 200 K in $T_{\rm eff}$, −0.03 ± 0.3 dex in [Fe/H], and −0.13 ± 0.35 in log g.

5.5 The Hertzsprung–Russell diagram

Fig. 8 shows the distribution of the HiVel stars in the colour-magnitude diagram (left-hand panel), and in the Kiel diagram (right-hand panel). The absolute magnitudes have been derived from *Gaia* DR3 magnitudes using the distances of Bailer-Jones et al. (2021). The effective temperatures and surface gravities in the Kiel diagram are the values obtained by the CNN algorithm. The curves in blue, orange, green, and red are the isochrones computed for metallicities −0.5, −1.0, −1.5, and −2.0 dex, respectively. The data for the isochrones have been generated using the PAdova and TRieste Stellar Evolution Code (PARSEC, Bressan et al. 2012).[16]

Most of the stars in the HiVel sample are in the red giant branch, and a few stars are in the turn-off region. Considering the stellar masses provided by the StarHorse catalogue (Anders et al. 2022), we compute the corresponding stellar radii using: (i) the values of log g from the StarHorse catalogue itself, and (ii) the values of log g predicted by our CNN model. The resulting radii are reported in Table 4, and they are compatible with stars of the red giant branch.

5.6 Chemical constraints

Detailed information on the chemical abundances in the atmospheres of the stars is relevant to constrain the places of origin of high velocity stars (chemical tagging). However, we do not have access to such information for the HiVel sample analysed here, so we can only discuss some constraints on their origin based on the position in the H–R diagram, the metallicities derived from J-PLUS data, and complementary chemical information that may be found in spectroscopic surveys or other sources (see Table 5).

As previously stated, the majority of the HiVel stars are in the red giant branch and three stars are in the turn-off region. The temperature range of the sample is between 4000 and 6000 K, which rules out the presence of runaway stars or white dwarf (WD) hyper-runaway stars in the sample ($T_{\rm eff}$ > 8000 K).

According to the metallicity values derived by the CNN, we have three stars with [Fe/H] ≥ −0.5 that have a chance of belonging to the

[15] http://cdsarc.u-strasbg.fr/viz-bin/cat/J/A+A/659/A181.

[16] http://stev.oapd.inaf.it/cmd/.

Downloaded from https://academic.oup.com/mnras/article/522/3/3898/7143802 by SBD-FFLCH-USP user on 21 August 2023

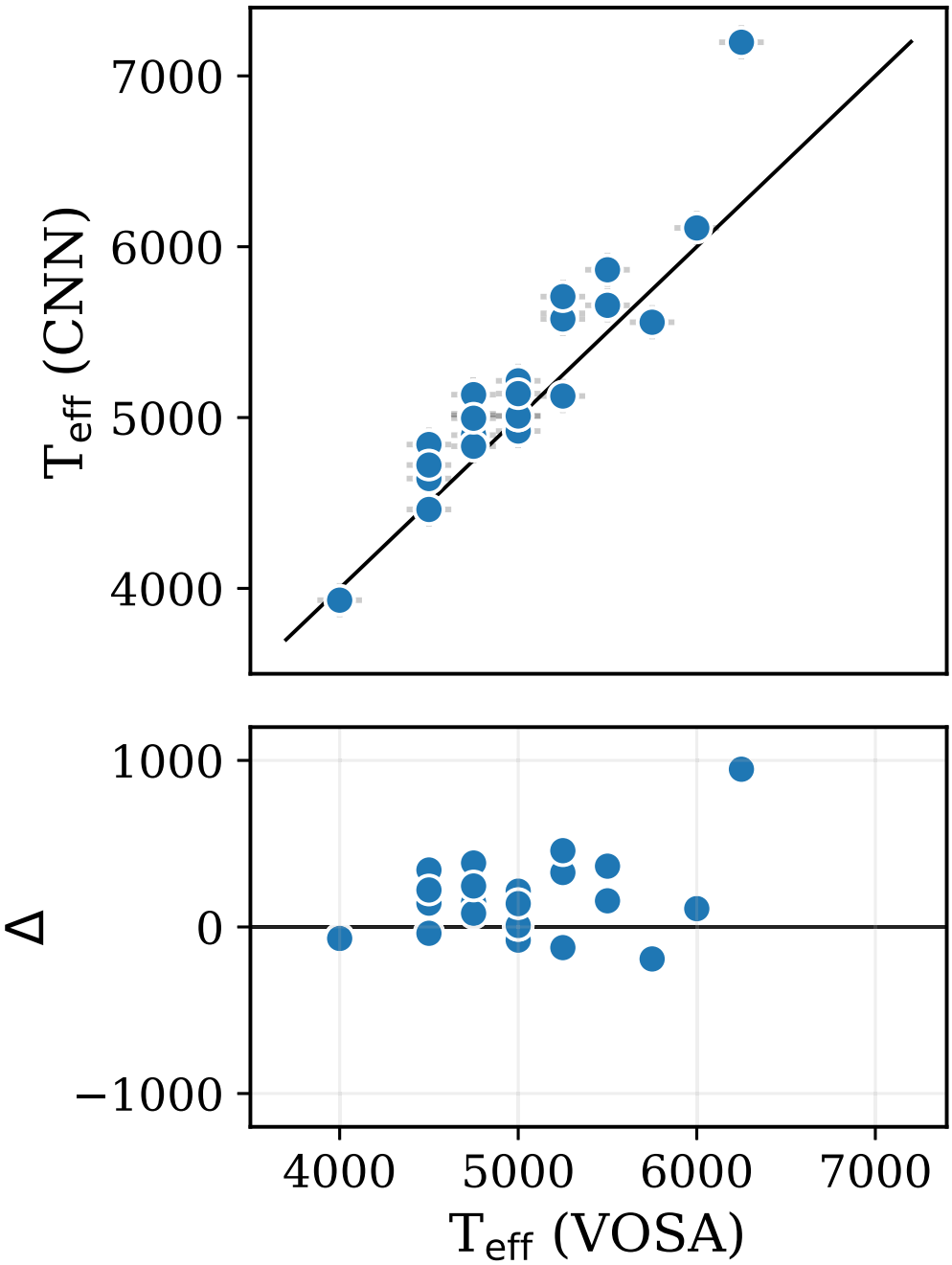

Figure 7. Comparison between the effective temperature determined by the CNN model and VOSA with model Kurucz ODFNEW /NOVER, alpha: 0.4 (2003), for our HiVel stars sample. The bottom panel shows the differences $\Delta = \mathrm{CNN} - \mathrm{VOSA}$.

thick or thin disks. Information on α-elements abundances is available for only two of these stars, *Gaia* DR3 1428 946 275 194 761 216 and *Gaia* DR3 1890 506 653 647 184 768 (Table 5). According to such abundances, these two stars would belong to the thin disk. Nevertheless, these abundances have been obtained from low resolution spectra and/or machine learning algorithms, and a high-resolution spectroscopic follow-up would be necessary to confirm them.

The remaining stars in our sample can be classified as metal-poor stars ([Fe/H] < -0.5), which is a characteristic expected for halo stars. Information on α-elements abundances is important to determine if the halo stars in the metallicity range $-2.0 <$ [Fe/H] < -0.5 were accreted from external stellar systems in the past (high-α abundances) or if they formed locally in our Galaxy (low-α abundances, Nissen & Schuster 2010). The abundances reported in Table 5 indicate that three stars fall in the high-α population, seven stars fall in the low-α population, and for two stars the information is inconclusive. Once again, we recall that these abundances come from low resolution spectra and/or machine learning algorithms, and may depend on systematic effects. Therefore, an analysis of all the HiVel stars using high-resolution spectra is necessary to draw definitive conclusions about their origins.

Downloaded from https://academic.oup.com/mnras/article/522/3/3898/7143802 by SBD-FFLCH-USP user on 21 August 2023

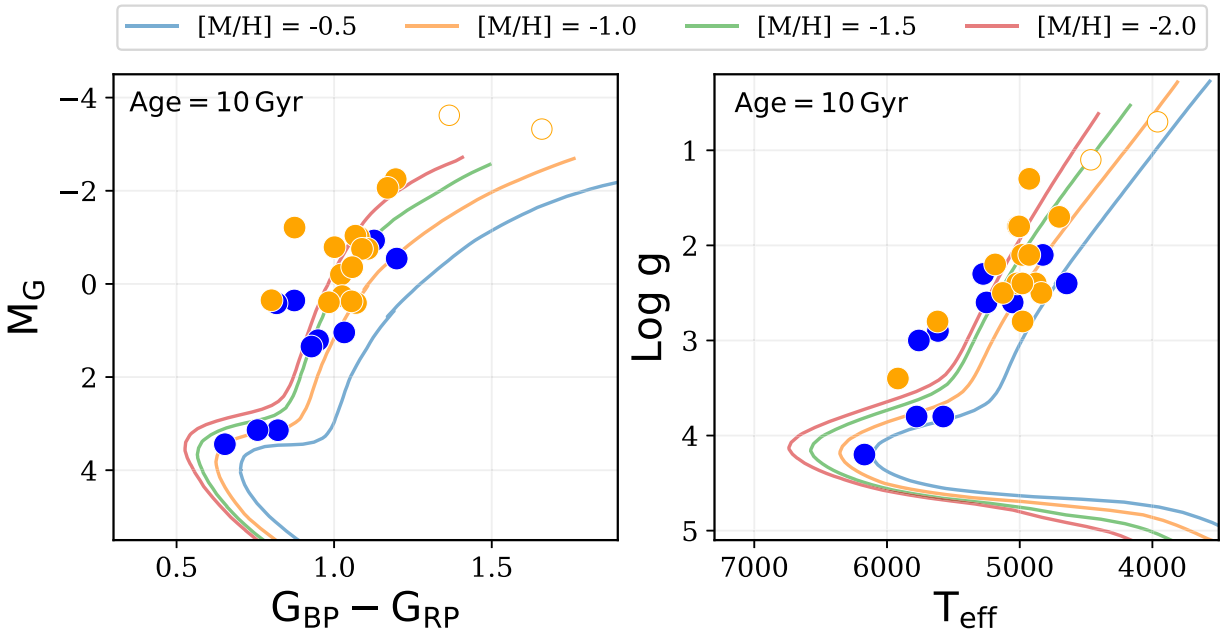

Figure 8. Location of the high velocity stars in the colour-magnitude diagram (left) using *Gaia* magnitudes, and in the Kiel diagram (right) using CNN values. The lines are isochrones computed for different metallicities (see text for details). Colour code is the same as in Fig. 1.

Table 4. Stellar masses from the StarHorse (SH) catalogue and estimated radii.

Gaia DR3 ID	SH Mass ($M_\odot$)	SH Radius ($R_\odot$)	CNN Radius ($R_\odot$)
1336 662 924 245 986 176	0.79	13.20	13.08
1342 335 888 849 476 864	0.85	5.92	7.63
1343 323 971 845 379 968	0.79	11.85	5.86
1395 639 113 051 405 824	0.78	8.32	5.20
1396 963 577 886 583 296	0.77	65.61	64.86
1399 596 186 680 287 616	0.83	17.94	19.00
1428 946 275 194 761 216	0.91	2.02	1.99
1565 897 801 417 595 136	0.79	8.26	2.93
1613 154 433 222 682 368	0.90	1.57	1.25
1774 483 437 903 554 944	0.88	2.24	1.95
1890 506 653 647 184 768	0.89	16.02	9.83
1901 537 847 650 215 424	0.86	9.86	9.69
2092 453 885 607 135 744	0.86	14.96	19.29
2104 759 069 985 260 416	0.85	15.63	8.60
2117 018 933 872 374 272	0.77	57.22	40.83
2117 987 431 816 799 104	0.78	16.89	13.03
2118 955 689 244 636 672	0.88	10.31	6.17
2154 188 852 160 448 512	0.78	18.59	13.05
2155 887 803 783 818 624	0.82	31.64	21.17
2266 761 044 499 471 488	0.78	7.73	4.63
2577 104 317 472 212 736	0.78	14.24	9.24
4570 724 026 270 780 416	0.84	9.39	8.50
4574 589 702 994 326 144	0.91	9.94	9.94
4601 980 530 506 725 888	0.86	5.48	10.83
4603 065 267 448 558 848	0.78	27.62	32.71
4609 671 373 825 731 584	0.83	9.10	11.95
4610 093 483 212 194 304	0.89	7.04	7.82

Table 5. Metallicity and α-elements abundance from other sources.

Gaia DR3 ID	[Fe/H]	[α/Fe]	Source
1 343 323 971 845 379 968	-1.39 ± 0.02	$+0.18 \pm 0.01$	b
1395 639 113 051 405 824	-1.65 ± 0.05	$+0.33 \pm 0.03$	c
1396 963 577 886 583 296	-0.80 ± 0.07	$+0.20 \pm 0.08$	d
1399 596186 680 287 616	-2.45 ± 0.07	$+0.25 \pm 0.04$	d
1428 946 275 194 761 216	-0.32 ± 0.03	$+0.03 \pm 0.02$	b
	-0.47 ± 0.07	$+0.18 \pm 0.08$	d
156 589 7801 417 595 136	-1.65 ± 0.02	-0.08 ± 0.01	b
	-1.68 ± 0.07	$+0.27 \pm 0.08$	d
1774 483 437 903 554 944	-1.41 ± 0.02	$+0.07 \pm 0.01$	b
1890 506 653 647 184 768	-0.21 ± 0.02	-0.02 ± 0.05	b
1901 537 847 650 215 424	-1.13 ± 0.07	$+0.16 \pm 0.08$	d
2117 018 933 872 374 272	-1.64 ± 0.02	$+0.08 \pm 0.02$	a
	-1.83 ± 0.04	$+0.41 \pm 0.03$	b
2577 104 317 472 212 736	-1.42 ± 0.07	$+0.02 \pm 0.03$	b
	-1.03 ± 0.07	$+0.17 \pm 0.08$	d
4574 589 702 994 326 144	-1.17 ± 0.07	$+0.25 \pm 0.08$	d
4601 980 530 506 725 888	-1.95 ± 0.05	$+0.16 \pm 0.02$	b
4603 065 267 448 558 848	-2.01 ± 0.07	$+0.07 \pm 0.08$	d

Notes. [a] APOGEE DR17.
[b] LAMOST DR7 Low-resolution spectra.
[c] LAMOST DR7 Medium-resolution spectra.
[d] CSNET.

6 CONCLUSIONS

In this work, we searched for and characterized 28 stars observed by the J-PLUS DR2 that, according to their astrometric solutions provided by the *Gaia* DR3 catalog, display Galactocentric velocities $> 400\,\mathrm{km\,s^{-1}}$. These high velocity (HiVel) stars do not exceed the escape velocity of the Galaxy, regardless of the potential model adopted, and we may discard the presence of any hyper-velocity (HVS) or hyper-runaways stars in the sample. This is an expected result, given that the detection rate of hyper-velocity stars in *Gaia*, considering recent measurements of the initial mass function and ejection rate in the Galactic center, is very low (Evans, Marchetti & Rossi 2022). Actually, we do not expect to find O-type stars with hypervelocity in our sample, taking into account that we use stars with radial velocity information in *Gaia* DR3 that is only available for stars with temperatures between 3100 and 14 500 K. Besides,

Downloaded from https://academic.oup.com/mnras/article/522/3/3898/7143802 by SBD-FFLCH-USP user on 21 August 2023

the detection of WD hyper-runaway stars in *Gaia* is not simple. For example, to find the three candidates with a high chance of being WD hyper-runaway stars reported by Shen et al. (2018), the authors performed a strategic search using *Gaia* DR2 astrometric data and radial velocities obtained from spectroscopy.

The kinematical and dynamical analyses applied to our sample indicate that high velocity stars with a possible origin in the Galactic center or in the LMC are ruled out. Nevertheless, this result might be sensitive to the galactic potential considered, both for the Milky Way and the LMC. The analyses allows us to conclude that all the stars are in the halo region, evolving on very eccentric orbits ($e > 0.6$) and reaching maximum heights well above the Galactic plane ($Z_{\max} > 10$ kpc). Recently, a large number of stars with these same kinematical characteristics have been reported (Hattori et al. 2018; Marchetti et al. 2019; Li et al. 2021; Quispe-Huaynasi et al. 2022), thus our HiVel sample could be part of such populations.

Being typical halo stars, the possible origin of the HiVel stars could be related to mergers of dwarf galaxies or globular cluster with the Milky Way in the past. In particular, the distribution in the actions diamond space indicate that some stars could belong to the Sequoia and to the *Gaia*-Enceladus/Sausage structures. These stars are important candidates for a more detailed study through high-resolution spectroscopy, both to confirm their radial velocities and to understand their chemical nature.

ACKNOWLEDGEMENTS

This work has been partially financed by the Coordenação de Aperfeiçoamento de Pessoal de Nível Superior, Brasil (CAPES)—Finance Code 001, and the Spanish Ministry of Science and Innovation—fund PID2021-124918NB-C42.

FR and CBP acknowledge financial support from the Brazilian National Council of Reserach (CNPq).

The work of VMP is supported by NOIRLab, which is managed by the Association of Universities for Research in Astronomy (AURA) under a cooperative agreement with the National Science Foundation.

FJE acknowledges financial support by ESA (SoW SCI-OO-SOW-00371).

AAC acknowledges financial support from the grant CEX2021-001131-S funded by MCIN/AEI/10.13039/501100011033.

AE acknowledges the financial support from the Spanish Ministry of Science and Innovation and the European Union—NextGenerationEU through the Recovery and Resilience Facility project ICTS-MRR-2021-03-CEFCA.

Based on observations made with the JAST/T80 telescope at the Observatorio Astrofísico de Javalambre (OAJ), in Teruel, owned, managed, and operated by the Centro de Estudios de Física del Cosmos de Aragón (CEFCA). We acknowledge the OAJ Data Processing and Archiving Unit (UPAD) for reducing and calibrating the OAJ data used in this work.

Funding for the J-PLUS Project has been provided by the Governments of Spain and Aragón through the Fondo de Inversiones de Teruel; the Aragón Government through the Research Groups E96, E103, and E16_17R; the Spanish Ministry of Science, Innovation and Universities (MCIU/AEI/FEDER, UE) with grants PGC2018-097585-B-C21 and PGC2018-097585-B-C22; the Spanish Ministry of Economy and Competitiveness (MINECO) under AYA2015-66211-C2-1-P, AYA2015-66211-C2-2, AYA2012-30789, and ICTS-2009-14; and European FEDER funding (FCDD10-4E-867, FCDD13-4E-2685). The Brazilian agencies FINEP, FAPESP, and the National Observatory of Brazil have also contributed to this project.

This work used VOSA, developed under the Spanish Virtual Observatory (https://svo.cab.inta-csic.es) project funded by MCIN/AEI/10.13039/501100011033/ through grant PID2020-112949GB-I00.

This work used of data from the European Space Agency (ESA) mission *Gaia* (https://www.cosmos.esa.int/gaia), processed by the *Gaia* Data Processing and Analysis Consortium (DPAC, https://www.cosmos.esa.int/web/gaia/dpac/consortium). Funding for the DPAC has been provided by national institutions, in particular the institutions participating in the *Gaia* Multilateral Agreement.

DATA AVAILABILITY

The data related to the results presented in this work and the trained CNN can be available on reasonable request to the corresponding author.

REFERENCES

Abadi M. G., Navarro J. F., Steinmetz M., 2009, ApJ, 691, L63
Abdurro'uf et al., 2022, ApJS, 259, 35
Aguado D. S. et al., 2021, ApJ, 908, L8
Allard F., Homeier D., Freytag B., 2011, in Johns-Krull C., Browning M. K., West A. A.eds, Astronomical Society of the Pacific Conference SeriesVol. 448, 16th Cambridge Workshop on Cool Stars, Stellar Systems, and the Sun, Astronomical Society of the Pacific, San Francisco, p. 91
Allen C., Santillan A., 1991, Rev. Mex. Astron. Astrofis., 22, 255
Allende Prieto C., 2016, A&A, 595, A129
Anders F. et al., 2022, A&A, 658, A91
Anguiano B. et al., 2018, A&A, 620, A76
Asplund M., Grevesse N., Sauval A. J., Scott P., 2009, ARA&A, 47, 481
Babusiaux C. et al., 2022, preprint (arXiv:2206.05989)
Bailer-Jones C. A. L., Rybizki J., Fouesneau M., Demleitner M., Andrae R., 2021, VizieR Online Data Catalog, p. I/352
Bastian N., Lardo C., 2018, ARA&A, 56, 83
Bayo A., Rodrigo C., Barrado Y Navascués D., Solano E., Gutiérrez R., Morales-Calderón M., Allard F., 2008, A&A, 492, 277
Bennett M., Bovy J., 2019, MNRAS, 482, 1417
Binney J., 2012, MNRAS, 426, 1324
Blaauw A., 1961, Bull. Astron. Inst. Neth., 15, 265
Bland-Hawthorn J., Gerhard O., 2016, ARA&A, 54, 529
Bonaca A. et al., 2021, ApJ, 909, L26
Bonoli S. et al., 2021, A&A, 653, A31
Boubert D., Erkal D., Gualandris A., 2020, MNRAS, 497, 2930
Bovy J., 2015, ApJS, 216, 29
Bressan A., Marigo P., Girardi L., Salasnich B., Dal Cero C., Rubele S., Nanni A., 2012, MNRAS, 427, 127
Brown W. R., 2015, ARA&A, 53, 15
Capuzzo-Dolcetta R., Fragione G., 2015, MNRAS, 454, 2677
Castelli F., Kurucz R. L., 2003, in Piskunov N., Weiss W. W., Gray D. F.eds, IAU Symp. 210, Modelling of Stellar Atmospheres, Poster Contributions, Astron. Soc. Pac., San Francisco, p. A20, preprint (arXiv:astro-ph/0405087)
Cenarro A. J. et al., 2014, in Proc. SPIEVol. 9149, Observatory Operations: Strategies, Processes, and Systems V, SPIE, Montréal, p. 91491I
Cenarro A. J. et al., 2019, A&A, 622, A176
Chollet F., et al., 2015, Keras, GitHub, https://keras.io
Cui X.-Q. et al., 2012, Res. Astron. Astrophys., 12, 1197
Drake A. J. et al., 2013, ApJ, 763, 32
Drimmel R., Poggio E., 2018, Res. Notes Am. Astron. Soc., 2, 210
Erkal D., Boubert D., Gualandris A., Evans N. W., Antonini F., 2019, MNRAS, 483, 2007
Evans F. A., Marchetti T., Rossi E. M., 2022, MNRAS, 512, 2350
Fragione G., Gualandris A., 2019, MNRAS, 489, 4543
Freeman K., Bland-Hawthorn J., 2002, ARA&A, 40, 487
Gaia Collaboration, 2022, preprint (arXiv:2208.00211)

Downloaded from https://academic.oup.com/mnras/article/522/3/3898/7143802 by SBD-FFLCH-USP user on 21 August 2023

Galarza C. A. et al., 2022, A&A, 657, A35
Gebran M., Connick K., Farhat H., Paletou F., Bentley I., 2022, Open Astron., 31, 38
Gravity Collaboration, 2018, A&A, 615, L15
Green G., 2018, J. Open Source Soft., 3, 695
Gualandris A., Portegies Zwart S., 2007, MNRAS, 376, L29
Hattori K., Valluri M., Bell E. F., Roederer I. U., 2018, ApJ, 866, 121
Hawkins K., Wyse R. F. G., 2018, MNRAS, 481, 1028
Heinze A. N. et al., 2018, AJ, 156, 241
Helmi A., 2020, ARA&A, 58, 205
Helmi A., White S. D. M., de Zeeuw P. T., Zhao H., 1999, Nature, 402, 53
Hills J. G., 1988, Nature, 331, 687
Horta D. et al., 2023, MNRAS, 520, 5671
Irrgang A., Wilcox B., Tucker E., Schiefelbein L., 2013, A&A, 549, A137
Katz D. et al., 2022, preprint (arXiv:2206.05902)
Keller S. C. et al., 2007, PASA, 24, 1
Kingma D. P., Ba J., 2015, in Bengio Y., LeCun Y.eds, 3rd International Conference for Learning Representations, DBLP Computer Science Bibliography, Trier, preprint (arXiv:1412.6980)
Koposov S. E. et al., 2020, MNRAS, 491, 2465
Lane J. M. M., Bovy J., Mackereth J. T., 2022, MNRAS, 510, 5119
Li Y.-B. et al., 2021, ApJS, 252, 3
López-Sanjuan C. et al., 2021, A&A, 654, A61
McMillan P. J., 2017, MNRAS, 465, 76
Marchetti T., Rossi E. M., Brown A. G. A., 2019, MNRAS, 490, 157
Marchetti T., Evans F. A., Rossi E. M., 2022, MNRAS, 515, 767
Marín-Franch A., Taylor K., Cenarro J., Cristobal-Hornillos D., Moles M., 2015, T80Cam: a wide field camera for the J-PLUS survey, in IAU General Assembly, Meeting #29, id. 2257381
Mendes de Oliveira C. et al., 2019, MNRAS, 489, 241
Monty S., Venn K. A., Lane J. M. M., Lokhorst D., Yong D., 2020, MNRAS, 497, 1236
Myeong G. C., Vasiliev E., Iorio G., Evans N. W., Belokurov V., 2019, MNRAS, 488, 1235
Naidu R. P., Conroy C., Bonaca A., Johnson B. D., Ting Y.-S., Caldwell N., Zaritsky D., Cargile P. A., 2020, ApJ, 901, 48
Nissen P. E., Schuster W. J., 2010, A&A, 511, L10
O'Malley T., Bursztein E., Long J., Chollet F., Jin H., Invernizzi L., et al., 2019, KerasTuner, GitHub, https://github.com/keras-team/keras-tuner
Oort J. H., 1922, Bull. Astron. Inst. Neth., 1, 133
Oort J. H., 1924, Proc. Natl. Acad. Sci., 10, 256
Oort J. H., 1926, Observatory, 49, 302
Poveda A., Ruiz J., Allen C., 1967, Bol. Obs. Tonantzintla y Tacubaya, 4, 86
Price-Whelan A., 2018, adrn/pyia: v0.2, Zenodo, Genève, https://zenodo.org/record/5057363
Przybilla N., Fernanda Nieva M., Heber U., Butler K., 2008, ApJ, 684, L103
Quispe-Huaynasi F. et al., 2022, AJ, 164, 187
Reggiani H., Ji A. P., Schlaufman K. C., Frebel A., Necib L., Nelson T., Hawkins K., Galarza J. Y., 2022, AJ, 163, 17
Rybizki J. et al., 2021, MNRAS, 510, 2597
Schlafly E. F., Finkbeiner D. P., 2011, ApJ, 737, 103
Sesar B. et al., 2017, AJ, 153, 204
Shen K. J. et al., 2018, ApJ, 865, 15
Shipp N. et al., 2021, ApJ, 923, 149
Starkenburg E. et al., 2017, MNRAS, 471, 2587
Whitten D. D. et al., 2019, A&A, 622, A182
Whitten D. D. et al., 2021, ApJ, 912, 147
Yang L. et al., 2022, A&A, 659, A181
Yanny B. et al., 2009, AJ, 137, 4377
Zwicky F., 1957, Morphological Astronomy. Springer Berlin, Heidelberg

This paper has been typeset from a TEX/LATEX file prepared by the author.

Downloaded from https://academic.oup.com/mnras/article/522/3/3898/7143802 by SBD-FFLCH-USP user on 21 August 2023

© 2023 The Author(s)
Published by Oxford University Press on behalf of Royal Astronomical Society